ORIGINAL ARTICLE

Journal Section

Control of Instabilities in Resonant Converters Using Half-Period Time Delay Output Feedback

Kuntal Mandal[1] | **Mohamed Al-Numay**[2] | **Zhen Li**[3] | **Abdelali El Aroudi**[1]

[1]Department of Electronics, Electrical Engineering and Automatic Control, Universitat Rovira i Virgili, Tarragona, Spain.

[2]Electrical Engineering Department, King Saud University, Riyadh, Saudi Arabia.

[3]School of Automation, Beijing Institute of Technology, Beijing, China.

Correspondence
Kuntal Mandal, Department of Electronics, Electrical Engineering and Automatic Control, Universitat Rovira i Virgili, Tarragona, Spain.
Email: dr.kuntal.mandal@gmail.com

Funding information
This work was funded by the Agency for Management of University and Research Grants (AGAUR) under the Ministry of Research and Universities of the Government of Catalonia (Grant Reference No. 2020 BP 00260).
Abdelali El Aroudi acknowledges the support from the Spanish Ministerio de Ciencia e Innovación under grant PID2023-150839OB-I00. Abdelali El Aroudi and Mohammed Al-Numay acknowledge financial support from the Researchers Supporting Project Number (RSP2024R150), King Saud University, Riyadh, Saudi Arabia.

Bifurcation phenomena in power electronic converters lead to undesired instabilities. In this paper different types of bifurcations are identified which can occur in a series load resonant converter with the variation of the parameters e.g., input voltage, load resistance, etc. These instabilities are associated mainly to three different bifurcations: (a) Neimark-Sacker, (b) Saddle-Node, and (c) Symmetry Breaking bifurcations. Due to the symmetry property of load resonant converters, a half-period time delay output feedback control is used to avoid all of these instabilities. The ideal time delay is realized by a first-order all-pass-filter. The stability analysis is performed and the values of the feedback gains are determined to identify the stable domain in the parameter space. By identifying the unstable orbits, the analytical stability analysis helps to understand as well as to control the mechanisms of these instabilities which extends the stability domain of the system. This study can also be extended to other load resonant converters where the symmetry property naturally exists.

KEYWORDS
Resonant DC-DC Converters, Symmetry, Soft Switching, Instability, Half Period Time Delay Control.

1 | INTRODUCTION

Power supplies from low to high ranges are widely applied in consumer electronics, servers, data centers, telecommunication systems. Compared to their conventional counterparts, the resonant converters are capable of providing small size, light weight, fast transient response, and high power density power supplies by virtue of their near-lossless soft switching techniques such as zero voltage switching (ZVS) or zero current switching (ZCS) [1]. In ZVS and ZCS techniques, either the voltage across the switch or the current through it is zero during the process of turning OFF or turning ON depending upon which variable is maintained at zero during switching. In contrast to the sharp-edged switching waveforms of PWM converters, implementing ZVS or ZCS resonant converter topologies require additional resonant elements to feature smooth waveforms resulting in reduced switching losses and less electromagnetic interference (EMI) at high switching frequency [2]. Recently, the increased proliferation of renewable energy sources (RESs) has also led to the significant scientific interest in energy-efficient processing circuit [3], used to facilitate the integration of RESs with the loads of different characteristics [4]. Among many, some of the examples are mentioned here such as electrical power systems [5], lighting systems, electrical vehicles [6] and their charging stations etc [7]. These power converters perform the task of conditioning the varying (and in many senses uncontrollable and stochastic nature) input conditions and power, matching them to the strict and narrow framework of load and grid regulations, in terms of voltage, frequency and power handling capability. It is therefore essential to have power electronics converters equipped with control schemes that are able to perform effectively and adequately under a wide spectrum of operating conditions. In contrast to the single-switch buck, boost or buck-boost DC-DC converters, the family of resonant DC-DC converters is vast and the diversity in resonant topologies gives the designer the freedom to choose the topology that most suits the application [8]. On the other hand, due to the large number of circuit topologies within a switching cycle and large number of operation modes, the analysis and control of resonant converters are complex [9].

Understanding the dynamics of resonant converters requires an appropriate model [10]. Modeling of these converters has attracted the interest of many researchers. Frequency-domain models based on first harmonic approximation (FHA) have been widely used for analyzing the existence and stability of the fundamental periodic orbit in resonant converters. FHA is an approximate technique derived from the harmonic balance approach [11]. The results derived from the FHA are valid only when the quality factor is sufficiently high and the operating frequency is close to the resonant one. Nonetheless, FHA is not accurate in predicting the system dynamics for low values of quality factor because strong nonlinearity effects appear in this case [12].

The switched model considering the switching dynamics is essential to unfold the different dynamical behaviors [13, 14]. As the number of subsystems are many in a switching cycle and operation modes are also large for input voltage and output load variation, the stability analysis is done by an automated algorithm [15, 16]. That is why the analysis of dynamics and different pathways to instabilities of vast family of resonant converters have been very few [17, 18, 19]. Namely, power electronic converters are nonlinear systems and can exhibit a great variety of nonlinear phenomena and bifurcation behaviors. Examples of such bifurcations are period doubling leading to subharmonic oscillations [20], Neimarck-Sacker bifurcation causing quasiperiodic behavior [21], border collision bifurcation causing a structural change in the system operation [22] and symmetry breaking causing coexistence of different solutions [18]. Different nonlinear behaviors are also reported for inverter circuits [23, 24, 25, 26]. The previous behaviors are undesired in a practical circuit and their control is of interest. Moreover the control of instabilities for this class of converters is rarely explored [27].

In the literature, there exist many control techniques to suppress bifurcation phenomena in nonlinear dynamical systems. The aim is by means of a specific feedback control action, the system dynamics is stabilized over the entire design parametric space of interest. One of the most known bifurcation control methods is the so-called time-delay feedback (TDF) control [28]. TDF stabilizes unstable periodic orbits (UPO) in nonlinear systems by shaping the frequency response of the controller and was applied to suppress subharmonic oscillation in DC-DC converters [29, 30, 31]. Filter-based controllers whose frequency response is an approximate of the one corresponding to TDF have been also shown to be capable to stabilize periodic orbits in power converters [32, 33, 34, 35]. The principle of stabilization is based on adding a perturbation term to the original control signal with the aim to modify the dynamic properties of the closed loop system and finally stabilizing it. In particular, for a nonlinear dynamical system $\dot{x} = f(x(t))$, the TDF adds in the feedback loop a new control input $\mu(t)$ that is expressed in terms of the error between a suitable output signal $y(t)$ and its τ_d-delayed version, *i.e* $\mu(t) = \kappa(y(t-\tau_d) - y(t))$ where κ is a feedback design parameter. In general, if the time delay τ_d is equal to the period of the UPO, this can be stabilized for values of κ within the stability domain [28]. However, it has been proved in [36] that for dynamical systems with odd symmetry, the TDFC cannot stabilize the the system. To overcome this limitation, the authors of [37] have proposed a modified TDFC called half-period time-delay (HPTD) feedback in which the delay time is equal to one half of the period of the UPO.

Though, there are broadly four types of resonant DC-DC converters, namely switch resonant [38], load resonant [39], resonant transition [40] and active-clamp [41] converters, only load resonant converter actively participating in the input-to-output power flow using a tank circuit. Depending on the number of reactive elements (two, three, four) and their configuration in the tank, there exist numerous resonant topologies with desirable control characteristics. In this paper a series load resonant converter with two reactive elements is studied. Considering only the fundamental harmonic of the series resonant converters, the approximate small-signal models [42] can not predict the fast-timescale instability. Based on the Filippov method, a generalized automated computational tool has been developed for time-domain stability analysis [13] and frequency-domain small-signal analysis [14] of DC-DC converters. In this method, the converters are analyzed by considering the switching actions explicitly and thus able to predict the fast-timescale dynamics. The existing controllers ([43, 44, 45, 46, 47, 48], and references therein) based on linear and nonlinear model have been proposed to improve the performance of the series resonant converters. But these controllers are not suitable to avoid or delay different types of instabilities with the variation of the parameters.

Two main contributions are given in this paper: first, using the nonlinear switched model of the series resonant DC-DC converters (Fig. 1) for various design specifications, different types of slow- and fast time-scale instabilities are identified with the variation of the parameters. Second, a half-period time delay (HPTD) feedback control is used, considering the symmetry in the waveforms, for the first time to avoid all of these instabilities, thus extending the parameter ranges for desired stable period-1 operation. Realization of the ideal delay is done by a first-order all-pass-filter. At present the design procedure of controller gains for time delay feedback involves time consuming brute-force simulation or experimentation over a large parameter range using commercial software. Using the newly developed tool [16], control domain of the feedback gains and stability curves in the parameter space are identified analytically.

The remainder of this paper is organized as follows. First, after this introduction, in Section 2 the system under study, a series load resonant converter, is presented and is further mathematically modeled in the same Section. In section 3 the control technique based on HPTD output feedback is applied to the system revealing its stabilizing effect. Section 4 deals with the system design in the parametric space where some applications of the HPTD output feedback are stated. Finally, conclusions are drawn in the last section.

2 | SERIES LOAD RESONANT CONVERTER

2.1 | Circuit Configuration and Operation

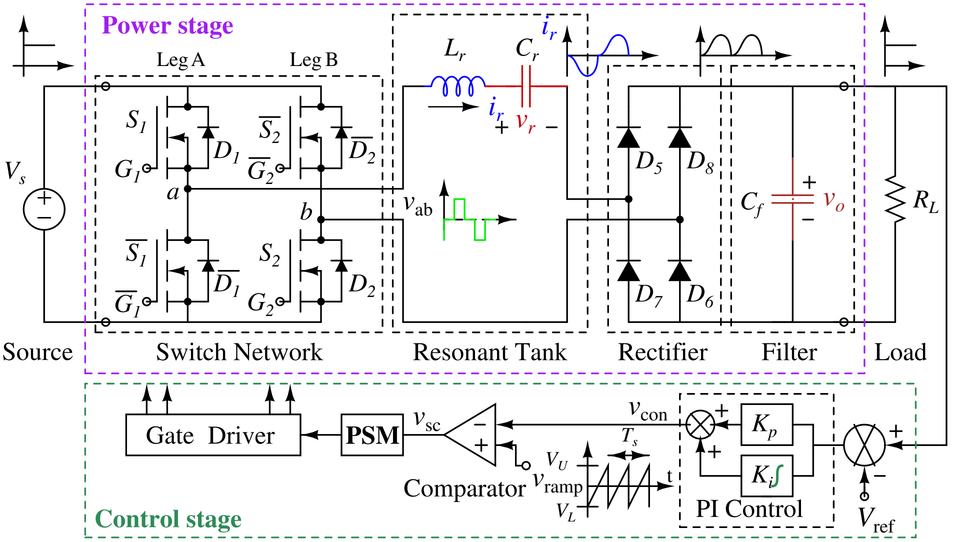

FIGURE 1 Circuit diagram of PI controlled phase shift modulated (PSM) series load resonant DC-DC converter (SRC). (color online)

Fixed frequency phase shift modulated (PSM) [49] control and series resonant converter (SRC) using PSM shown in Fig. 1 have been an emerging topic [42], and references therein). Like all other load resonant converters it uses a resonant tank which consists of an inductor L_r and a capacitor C_r operating in series resonance. The resulting resonant tank has a resonant frequency $f_r = 1/2\pi\sqrt{L_r C_r}$ and characteristic impedance $Z_0 = \sqrt{L_r/C_r}$. The lagging power factor mode operation can be achieved when the switching frequency is above the resonant frequency as $f_s > f_r$. For a half-period, the two switch states in the same leg are complementary and the switches in the diagonal locations are phase shifted. Since the input voltage is applied to the resonant tank only when both of the switches in the diagonal locations are turned ON, a pulse-width-modulated quasi-square wave voltage v_{ab} with duty ratio $d = \frac{T_{on}}{T_h}$ is generated across a and b (Fig. 3(a)). An almost sinusoidal current is produced after the voltage v_{ab} is fed to resonant tank. This current is rectified by an uncontrolled diode bridge rectifier and is filtered using C_f to get the required DC voltage across the load resistance R_L. The output voltage regulation for load (or line) variation is obtained by modulation of the duty ratio which is adjusted by T_{sft} shown in Fig. 3(a).

In order to illustrate the control mechanism, the block diagram of the conventional PSM block is shown in Fig. 2(a). The gating signals to the switch network from this block is shown in Fig. 2(b). The gating signals of leg A are ON at the start of each ramp cycle of time period T_h, and freely toggle at the middle of the switching period T_s. Hence, the period of the ramp wave T_h is half of the switching period Ts i.e., $T_h = \frac{T_s}{2} = \frac{1}{2f_s}$. The gating signals for the switch pair of leg B are shifted with respect to leg A by a time period T_{sft}. So, the switches in the diagonal locations are phase shifted. Since the input voltage is applied to the resonant tank only when both of the switches in the diagonal locations are turned on, a quasi-square wave v_{ab} is generated. The load voltage regulation for load (or line) variation

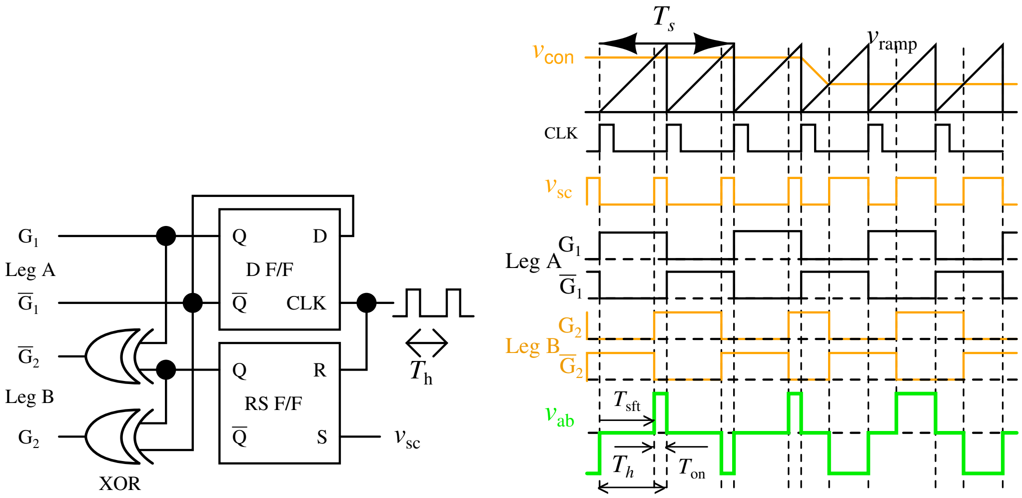

(a) (b)

FIGURE 2 (a) Schematic diagram of conventional PSM block (b) The gating signals to the H-bridge switches network from a conventional PSM block, showing a transition from one duty ratio to another in response to a load or line disturbance. (color online)

is obtained by adjusting T_{sft} or the duty ratio ($D = \frac{T_{on}}{T_h}$). Whenever the control signal v_{con} is greater than the ramp waveform, the switch signal v_{sc} is low. $\overline{S}_2$ and S_2 are turned OFF and ON successively, using the switch control signal v_{sc}. In one T_h period of the ramp wave, if v_{sc} is low then S_2 turns OFF, and in the next T_h half cycle if v_{sc} is low $\overline{S}_2$

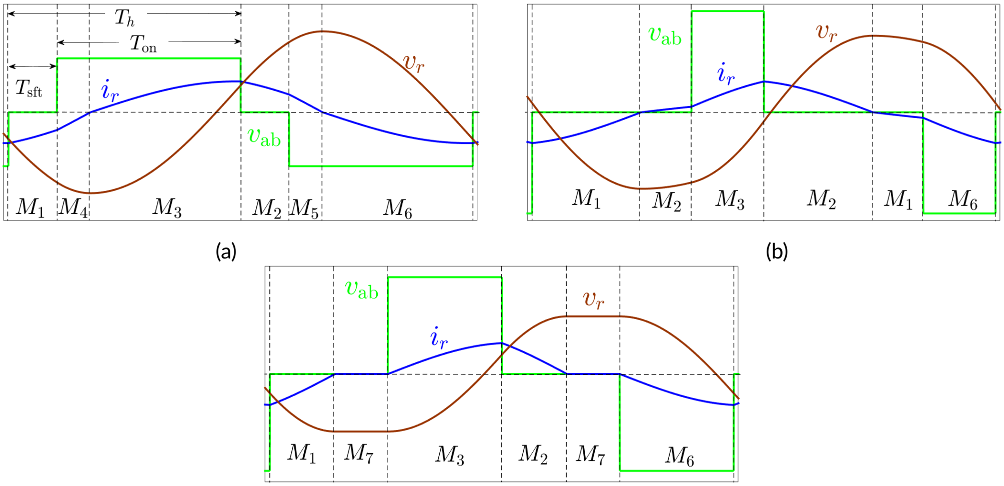

(a) (b)

(c)

FIGURE 3 Typical steady-state period-1 symmetric waveforms for nominal operation modes (a) Mode-I, (b) Mode-II, and (c) Mode-III in one switching period. Each operation mode consists of many topological modes or subsystems (M_i) in periodical sequence. (color online)

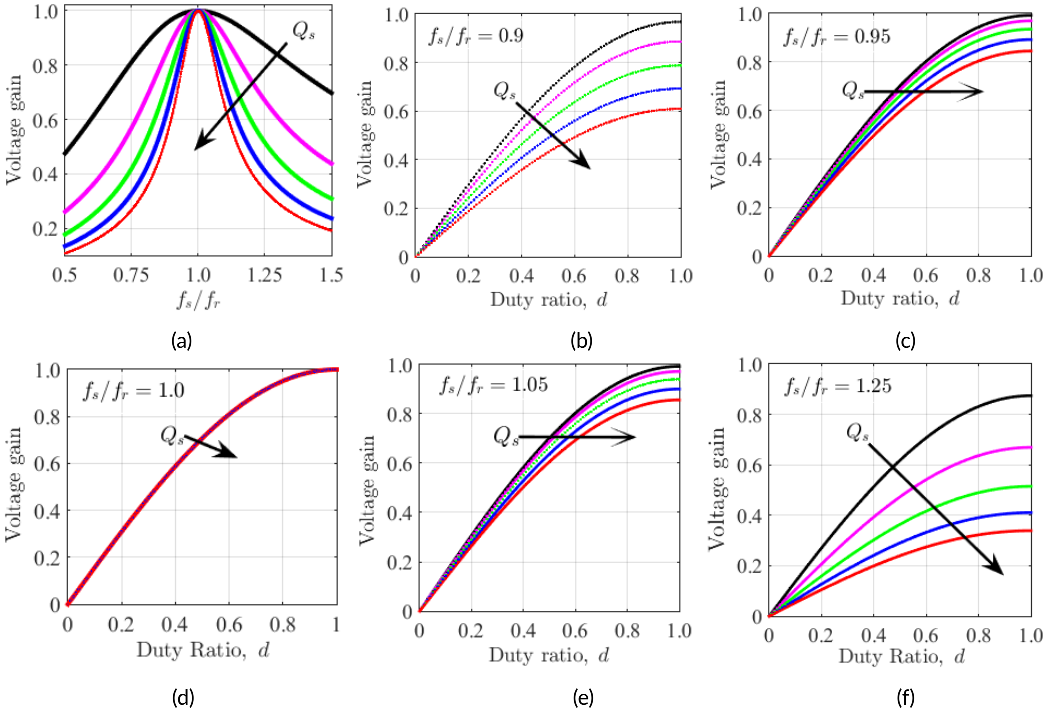

(a) (b) (c)

(d) (e) (f)

FIGURE 4 Voltage gain versus (a) normalized switching frequency and duty ratio at (b) $f_s/f_r = 0.9$, (c) $f_s/f_r = 0.95$, (d) $f_s/f_r = 1.0$, (e) $f_s/f_r = 1.05$, (f) $f_s/f_r = 1.25$. The Quality factor Q_s is varying from 1 (black) to 5 (red). (color online)

turns OFF. Otherwise these switches are ON. Note that no switching occurs when $v_{\text{con}} > V_U = -V_L$ within T_h, where the V_U and V_L are the upper and lower threshold voltages of the ramp.

Depending on the conduction states of the four controlled switches (with anti-parallel diodes) in the H-bridge (Fig. 1), this converter possesses nine subsystems or topological modes ($M_1 - M_9$) which can form many operation modes. But, for most practical applications [42], only three nominal operation modes hereafter called Mode-I, Mode-II, and Mode-III shown in Fig. 3 are used. When the conduction states of the switches forms the topological sequence $M_1 - M_4 - M_3 - M_2 - M_5 - M_6$ (Mode-I) the circuit provides moderate gain (Fig. 4(a)) and ZVS is easily achievable (Fig. 3(a)). A high quality factor ($Q_s = Z_0/R_L$) or high f_s/f_r ratio (Fig. 4(f)) results in Mode-I operation.

As shown in Fig. 3(b), in the topological sequence $M_1 - M_2 - M_3 - M_2 - M_1 - M_6$ (Mode-II) the circuit provides high (Fig. 4(c)) and moderate (Fig. 4(b)) gain and ZCS for both the legs. It is interesting to note that at $f_s/f_r = 1.0$, the duty ratio is unchanged with the variation of load (Fig. 4(d)) though the condition is very difficult to achieve practically. Mode-II operation is achieved by selecting a lower $\frac{f_s}{f_r}$. At lower load (i.e., higher R_L), operation in Mode-II is lost and Mode-III (Fig. 3(c)) is initiated. In Mode-III ($M_1 - M_7 - M_3 - M_2 - M_7 - M_6$), there is a subsystem M_7 where the resonant inductor current is zero. In this case, the so-called discontinuous conduction mode (DCM) takes place in each half cycle. Therefore, operation modes Mode-II and Mode-III are called continuous current mode (CCM) because resonant inductor current i_r is nonzero in each topological mode.

2.2 | State-Space Modeling

The PSM controlled SRC with ideal components in Fig. 1 can be described by the following set of differential equations

$$\begin{aligned}
\frac{di_r}{dt} &= \frac{1}{L_r}\left(-v_r - v_o\mathrm{sign}(i_r) + v_{\mathrm{ab}}\right),\\
\frac{dv_r}{dt} &= \frac{i_r}{C_r},\\
\frac{dv_0}{dt} &= \frac{1}{C_f}\left(|i_r| - \frac{v_o}{R_L}\right),\\
\frac{d\rho_i}{dt} &= K_i\left(v_o - V_{\mathrm{ref}}\right)
\end{aligned} \tag{1}$$

where sign stands for the *signum* function. In the above equations, there are two nonsmooth terms: sign and $|\cdot|$. As shown in Fig. 5(a), depending on the values of voltage v_{ab} and resonant current i_r, at most nine subsystems ($M_1 - M_9$) are possible. For example, M_1 in Fig. 5(a) is denoted by $v_{\mathrm{ab}} = 0$ and $i_r < 0$ which corresponds to the subsystem M_1 in Fig. 3(a). Similarly, M_3 in Fig. 5(a) is denoted by $v_{\mathrm{ab}} > 0$ and $i_r > 0$ which corresponds to the subsystem M_3 in Fig. 3(a). M_7 indicates voltage $v_{\mathrm{ab}} = 0$ and resonant current $i_r = 0$ (Fig. 3(c)).

All subsystems can be expressed in vector-matrix form as

$$M_i : \frac{d\boldsymbol{x}}{dt} = \boldsymbol{A}_i\boldsymbol{x} + \boldsymbol{B}_i\boldsymbol{u}, i = 1\cdots 9 \tag{2}$$

where $\boldsymbol{x}$ is the vector of the state variables and $\boldsymbol{u}$ is the vector of input parameters that are given by

$$\boldsymbol{x} = [\, i_r \;\; v_r \;\; v_o \;\; \rho_i \,]^\top = [\, x_1 \;\; x_2 \;\; x_3 \;\; x_4 \,]^\top,\ \boldsymbol{u} = [\, V_s \;\; V_{\mathrm{ref}} \,]^\top.$$

For subsystem M_1, $x_1 < 0$ and $v_{\mathrm{ab}} = 0$, therefore the matrices $\boldsymbol{A}_1$ and $\boldsymbol{B}_1$ in the differential equations (1) are given by

$$\boldsymbol{A}_1 = \begin{bmatrix} 0 & -\frac{1}{L_r} & -\frac{1}{L_r} & 0 \\ \frac{1}{C_r} & 0 & 0 & 0 \\ -\frac{1}{C_f} & 0 & -\frac{1}{R_L C_f} & 0 \\ 0 & 0 & K_i & 0 \end{bmatrix},\ \boldsymbol{B}_1 = \begin{bmatrix} 0 & 0 \\ 0 & 0 \\ 0 & 0 \\ 0 & -K_i \end{bmatrix}.$$

Symmetry in the waveforms (Fig. 3) gives a useful relationship among the matrices appearing in the different subsystems of equation (2): $\boldsymbol{A}_1 = \boldsymbol{A}_4 = \boldsymbol{A}_6,\ \boldsymbol{A}_2 = \boldsymbol{A}_3 = \boldsymbol{A}_5,\ \boldsymbol{A}_7 = \boldsymbol{A}_8 = \boldsymbol{A}_9,\ \boldsymbol{B}_1 = \boldsymbol{B}_2 = \boldsymbol{B}_7,\ \boldsymbol{B}_3 = \boldsymbol{B}_4 = \boldsymbol{B}_8,\ \boldsymbol{B}_5 = \boldsymbol{B}_6 = \boldsymbol{B}_9$.

To reduce the complexity of the computations further, projection matrices $\boldsymbol{W}_c$ and $\boldsymbol{W}_d$ for CCM and DCM operations are defined as $\boldsymbol{W}_c\boldsymbol{W}_c = \boldsymbol{I}$, where $\boldsymbol{W}_c$, $\boldsymbol{I}$ and $\boldsymbol{W}_d$ are given by

$$\boldsymbol{W}_c = \begin{bmatrix} -1 & 0 & 0 & 0 \\ 0 & -1 & 0 & 0 \\ 0 & 0 & 1 & 0 \\ 0 & 0 & 0 & 1 \end{bmatrix},\ \boldsymbol{I} = \begin{bmatrix} 1 & 0 & 0 & 0 \\ 0 & 1 & 0 & 0 \\ 0 & 0 & 1 & 0 \\ 0 & 0 & 0 & 1 \end{bmatrix},\ \boldsymbol{W}_d = \begin{bmatrix} 0 & 0 & 0 & 0 \\ 0 & -1 & 0 & 0 \\ 0 & 0 & 1 & 0 \\ 0 & 0 & 0 & 1 \end{bmatrix}.$$

Using these projection matrices, we have the relations $\boldsymbol{A}_2 = \boldsymbol{W}_c\boldsymbol{A}_1\boldsymbol{W}_c$, $\boldsymbol{A}_7 = \boldsymbol{W}_d\boldsymbol{A}_1\boldsymbol{W}_d$ and $\boldsymbol{B}_6 = \boldsymbol{W}_c\boldsymbol{B}_3$. Where, $\boldsymbol{B}_3$ and

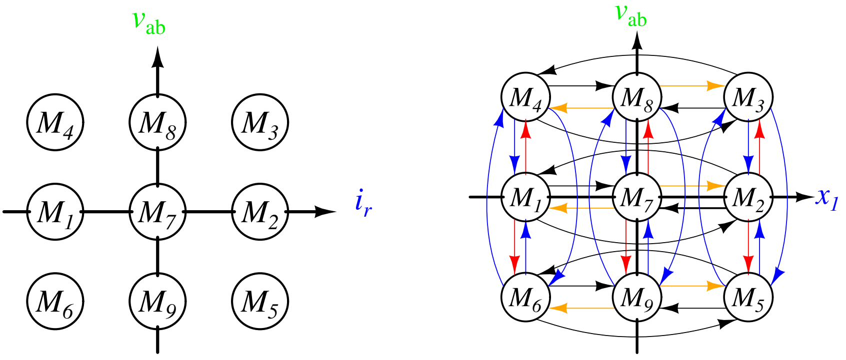

(a)

(b)

FIGURE 5 (a) Different subsystems depending on the positive, negative, and zero values of voltage v_{ab} and resonant inductor current i_r i.e., state variable x_1. (b) All possible transitions among subsystems assuming one switching at a time. The color code of switching conditions are: h_1-blue, h_2-orange, h_3-black, h_4-brown. (color online)

$\boldsymbol{B}_6$ are given by

$$\boldsymbol{B}_3 = \begin{bmatrix} \frac{1}{L_r} & 0 \\ 0 & 0 \\ 0 & 0 \\ 0 & -K_i \end{bmatrix}, \; \boldsymbol{B}_6 = \boldsymbol{W}_c \boldsymbol{B}_3 = \begin{bmatrix} -\frac{1}{L_r} & 0 \\ 0 & 0 \\ 0 & 0 \\ 0 & -K_i \end{bmatrix}.$$

From a “hybrid system” point of view, the four dimensional state-space is divided into nine subsystems (as given in Fig. 5(a)) by four switching surfaces. All possible transitions among subsystems are depicted in Fig. 5(b). For each subsystem there are four transitions to other subsystems. These transition can be either state- or time-dependent. Therefore, the 36 possible transitions between subsystems are categorized as 24 state-dependent transitions (h_1, h_2, h_4) and 12 time-dependent transitions (h_3). For the nominal stable symmetric period-1 waveforms (Fig. 3), the consideration of half-cycle dynamics i.e., half the number of subsystem sequence is sufficient [17]. But symmetry between half-cycles will break beyond the stability boundary of nominal period-1 operation. Therefore, for the study of different types of instabilities, the detection of all possible transitions between subsystems is needed depending on the switching conditions (Fig. 5(b)). It shows that for each subsystem there are 4 transitions to other subsystems and therefore there are 36 possible transitions between subsystems. Among them 24 are state-dependent transitions (shown in blue, red and orange arrow) and 12 are time-dependent transitions (shown in black arrow).

There are three kinds of switchings in each half cycle of the CCM operation (Fig. 3(a)): those determined by the resonant inductor current reaching zero (h_1), those by the intersection of the control voltage ($v_{\text{con}} = K_p(x_3 - V_{\text{ref}}) + x_4$) with the ramp voltage ($v_{\text{ramp}}(t) = V_L + (V_U - V_L)(t \mod T_h)$) and those at the end of each ramp cycle (h_3). In the DCM operation (Fig. 3(c)), there is another switching at the end of the zero inductor current interval of the resonant inductor (h_4). All the switching conditions for CCM and DCM are given by:

$$\begin{aligned} h_1 : x_1 = 0, \quad h_2 : v_{\text{con}} - v_{\text{ramp}} = 0, \\ h_3 : t \mod T_h = 0, \quad h_4 : x_3 - abs(x_2) = 0. \end{aligned} \tag{3}$$

3 | DYNAMICAL ANALYSIS METHODOLOGY

In this paper the time-domain stability analysis and frequency domain small-signal analysis have been done using the Filippov method which considers the switching action explicitly.

The stability of the system is given by the state transition matrix over the complete period (called the monodromy matrix), which comprises the state transition matrices across each subsystem, and the state transition matrices across the switching events (called saltation matrices). The eigenvalues of this monodromy matrix are called the Floquet multipliers. So long as all the Floquet multipliers are inside the unit circle, the system is stable. Various types of instabilities or bifurcations are characterised by where the Floquet multipliers exit the unit circle. The period doubling bifurcation is characterised by one Floquet multiplier being -1, the Neimark–Sacker bifurcation is characterised by a pair of complex conjugate multipliers having an absolute value of 1, and cyclic-fold symmetry breacking bifurcation is characterized by disappearence of a pair of periodic orbits being one of the multipliers equal to 1 at the bifurcation point .

On the other hand, the design of linear controller parameters of resonant converters is traditionally carried out by generalized averaging method (also called multiple-frequency averaging method) [50], equivalent circuit model [51] and extended describing function (EDF) technique [52]. In all these methods, the number of harmonics required to get accurate results depends on the resonant converter configuration, ratio of the switching frequency to the resonance frequency or pulse width.

Here, the quantitative dynamical analysis is done by a general automated computational tool [16] regardless of the order of resonant topology, linear control (fixed frequency (or duty-cycle control) or variable frequency control), single-loop or multi-loop feedback, continuous or discontinuous conduction mode, transition of different operation modes and the number of subsystems in one switching cycle.

3.1 | Time-Domain Stability Analysis and Selection of Controller Parameters

Thus, if a system goes through six subsystems in a periodic orbit with six transitions between them as given in Fig. 3(a), then the monodromy matrix is simply obtained as the matrix product

$$\mathbf{\Phi}_{\text{period}} = \mathbf{S}_{6,1} \cdot \mathbf{\Phi}_6 \cdot \mathbf{S}_{5,6} \cdot \mathbf{\Phi}_5 \cdot \mathbf{S}_{2,5} \cdot \mathbf{\Phi}_2 \cdot \mathbf{S}_{3,2} \cdot \mathbf{\Phi}_3 \cdot \mathbf{S}_{4,3} \cdot \mathbf{\Phi}_4 \cdot \mathbf{S}_{1,4} \cdot \mathbf{\Phi}_1 \tag{4}$$

where $\mathbf{\Phi}_i$ is the state transition matrix across the ith subsystem (given by an exponential matrix if the subsystem is linear time-invariant), and $\mathbf{S}_{i,j}$ is the saltation matrix for transition from subsystem i to subsystem j (i.e., across the switching event). The saltation matrix $\boldsymbol{S}_{i,j}$ is given by [19]):

$$\boldsymbol{S}_{i,j} = \Phi(t_{i,j}^{+}, t_{i,j}^{-}) = \boldsymbol{I}_n + \frac{[\, \boldsymbol{f}_j(\boldsymbol{x}_{i,j}, t_{i,j}) - \boldsymbol{f}_i(\boldsymbol{x}_{i,j}, t_{i,j}) \,]\, \boldsymbol{n}_{i,j}^{\mathsf{T}}}{\boldsymbol{n}_{i,j}^{\mathsf{T}}\, \boldsymbol{f}_i(\boldsymbol{x}_{i,j}, t_{i,j}) + \frac{\partial h_{i,j}}{\partial t}\big|_{t=t_{i,j}}} \tag{5}$$

where $\boldsymbol{I}$ is the identity matrix with appropriate dimension, $\boldsymbol{f}_i = \boldsymbol{A}_i\boldsymbol{x} + \boldsymbol{B}_i\boldsymbol{u}$ denotes vector field and $\boldsymbol{x}_{i,j}$ denotes the state at switching instant $t_{i,j}$ after satisfying the switching surface $h_{i,j} = 0$. The normal to the switching surface is denoted by $\boldsymbol{n}$, and the superscript $^{\mathsf{T}}$ denotes transpose operation. In the switching events that are given in a fixed pattern (e.g., controlled by a clock), the saltation matrix turns out to be the identity matrix.

Once the periodic orbit (and hence the switching instants) is known, this matrix can be calculated and from that, the Floquet multipliers can be extracted. Thus, one can obtain a direct and accurate estimation of the stability of the

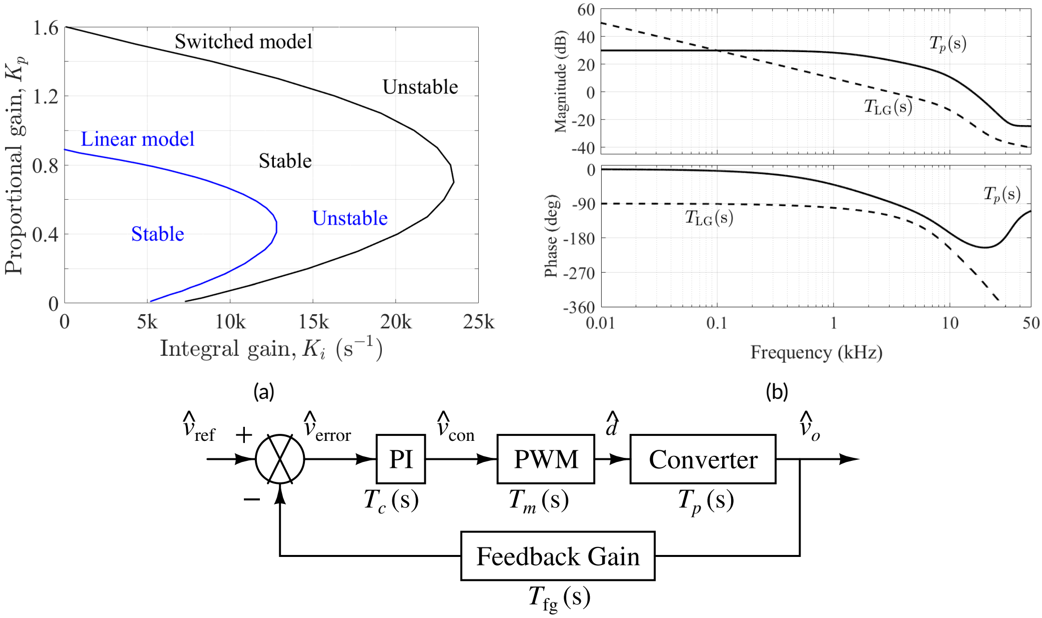

(a) (b)

(c)

FIGURE 6 (a) Boundary between stable and unstable regions in the $K_p - K_i$ parameter space for closed-loop switched (black) and linear (blue) model. The left side of the curves represents the zones of stability. (b) The Bode plot of the control-to-output voltage transfer function $T_p(s)$ (with duty-ratio $d = 0.4$) and loop gain transfer function (given in (11)) of the PSM controlled SRC. The parameters for the loop gain transfer function ($T_{\rm LG}(s)$) are given in Table 1 with $K_p = 0.25$, $K_i = 2500\ s^{-1}$. (c) transfer function block diagram of the closed-loop system.

system and how this changes with the variation of the system parameters.

According to the previous procedure, we have to set the values of proportional gain K_p and integral gain K_i for stable operation of the closed-loop system. We start by setting some initial values of the controller parameters K_p and K_i, and check for stability of the orbit. Once a stable periodic orbit is detected, it can be followed as the parameter is varied. Keeping K_p fixed, for a slightly different parameter value of K_i. With the increasing value of K_i, when the absolute value of the maximum eigenvalue lies on the unit circle, the parameters (K_p and K_i) are stored.

Thus the whole $K_p - K_i$ parameter-space is spanned, and subdivided into two parts, i.e., stable (left side of the boundary line) and unstable (right side of the boundary line). Such boundary lines are obtained for four different sets of input voltage and load conditions namely low line high load, low line low load, high line low load and high line high load. Among them the worst case condition is selected for choosing the controller parameters when the stability region is the smallest one. Choosing the controller parameters from this stable region, the system will be stable for the specified input voltage and load variation range. For example, this method is carried out for the design specification given in Table 1 with $V_s = 32$ V and $R = 6\ \Omega$ and stability cure is obtained for switched model as shown in Fig. 6(a).

3.2 | s-Domain Small-Signal Analysis and Stability Curve for Controller Parameters

The small-signal analysis of the converter starts by locating a periodic steady-state in open-loop in continuous time. Then, the small-signal model of the converter is found by giving small perturbation to the nominal control input (e.g., duty-ratio), input voltage, load current etc, and linearizing around the periodic steady-state. After obtaining the linearized small-signal model, the transfer functions of the system are derived in 's' domain by Laplace transformation. The small-signal transfer functions in open-loop are useful for prediction of the closed-loop behavior and for controller design of the switching converter. Among them, the control-to-output transfer function is used to predict the margin of stability of the closed-loop switching converter. Using the Bode plot, stability criteria of closed-loop system can be interpreted by measuring of the gain margin and phase margin.

Now the small-signal analysis is carried out for the design specification given in Table 1. For the worst case condition i.e., high line and low load ($V_s = 32$ V and $R = 6\,\Omega$), periodic orbit of the Mode-II is detected with nominal duty ratio $d = 0.4$. For Mode-II, in open-loop operation (without PI controller) first three equations are taken from (1). The switching instances $t_{1,2}$ and $t_{2,1}$ are not known *a priori* but the others are known. This gives $\boldsymbol{S}_{2,3} = \boldsymbol{S}_{3,1} = \boldsymbol{S}_{1,6} = \boldsymbol{S}_{6,1} = \boldsymbol{I}_3$, where $\boldsymbol{I}_3$ denotes three-dimensional identity matrix. To start the small-signal analysis we must find sampled state at the beginning of a switching cycle $\boldsymbol{X}^*$ and the two unknown switching instants. From the numerical solution we get $\boldsymbol{X}^* = [-1.8785\ 9.2347\ 6.4473]^\mathsf{T}$, and $t_{1,2} = 0.3366\,T_s$, $t_{2,1} = 0.8366\,T_s$. The small-signal model in the discrete-time domain can be expressed as follows

$$\hat{\boldsymbol{x}}_{n+1} = \boldsymbol{J}\hat{\boldsymbol{x}}_n + \Gamma_{T_k}\hat{d}_n \qquad (6)$$

$$\hat{v}_{o,n} = \mathbf{C}^\mathsf{T}\hat{\boldsymbol{x}}_n \qquad (7)$$

where the involved matrices are given by

$$\boldsymbol{J} = \boldsymbol{\Phi}_{6,OL} \times \boldsymbol{\Phi}_{1,OL} \times \boldsymbol{S}_{2,1,OL} \times \boldsymbol{\Phi}_2 \times \boldsymbol{\Phi}_{3,OL} \times \boldsymbol{\Phi}_{2,OL} \times \boldsymbol{S}_{1,2,OL} \times \boldsymbol{\Phi}_{1,OL} \qquad (8)$$

$$\Gamma_{T_k} = \boldsymbol{\Phi}_6 \times \left[\boldsymbol{f}_5(\boldsymbol{x}_{5,6}, t_{5,6}) - \boldsymbol{f}_6(\boldsymbol{x}_{5,6}, t_{5,6})\right] \qquad (9)$$

The discrete-time control-to-output transfer function in z-domain is calculated as

$$T_p(z) = \frac{\hat{v}_o}{\hat{d}}(z) = \mathbf{C}^\mathsf{T} \times (z\boldsymbol{I}_3 - \boldsymbol{J})^{-1}\boldsymbol{\Gamma}_{T_k} = \frac{0.54167(z+3.03)(z+0.7387)}{(z-0.8286)(z^2-0.5125z+0.2104)} \qquad (10)$$

Now replacing $z = e^{sT_s}$ and using the equivalent hold $\boldsymbol{H}(s)$, the continuous-time transfer function $T_p(s)$ is calculated [14] and the resulting Bode plot is shown in the Fig. 6(b). From Fig. 6(c), the loop gain transfer function is given as

$$T_{\mathrm{LG}}(s) = T_c(s)\,T_m(s)\,T_p(s)\,T_{\mathrm{fg}}(s) \qquad (11)$$

where, $T_c(s) = K_p + K_i/s$, $T_m(s) = 1/(V_U - V_L)$, $T_{\mathrm{fg}}(s) = 1$. Though the open-loop converter without controller is unstable, the system is stable with the PI controller (gain margin = 9.44 dB, phase margin = 58.7°) as shown in Fig. 6(b).

Now, using the closed-loop transfer function in s-domain, the $K_p - K_i$ parameter space is divided into the stable and unstable regions as shown in 6(a). Note that the system is stable for a larger range of the controller parameters compared to that predicted by the linear model (blue line). Thus, we select the controller gains as $K_p = 1$, $K_i = 5000\ s^{-1}$.

4 | HALF-PERIOD TIME-DELAY FEEDBACK CONTROL

As shown in Fig. 1, the control voltage using conventional PI controller is $v_{\mathrm{con}} = K_p(v_o(t) - V_{\mathrm{ref}}) + \rho_i(t)$, where, $\rho_i(t) = K_i\int(v_o(t) - V_{\mathrm{ref}})dt$ is the extra state variable due to the integral action. Using the half-period time delay

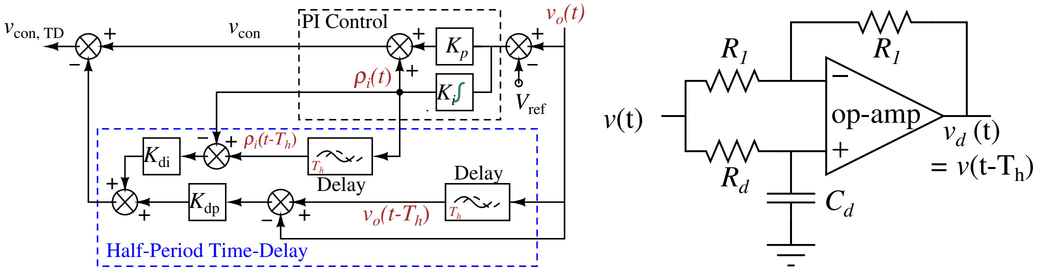

(a) (b)

FIGURE 7 (a) Half-Period Time Delay (HPTD) Control Block using two state variables $v_o(t)$ and $\rho_i(t)$. The Half period is denoted by $T_h = \frac{T_s}{2} = \frac{1}{2f_s}$. (b) realization of the delay by first-order all pass filter (APF) where $T_h = R_d C_d$. (color online)

(HPTD) feedback (Fig. 7(a)), the control voltage is modified as follows

$$v_{\text{con,TD}} \;=\; v_{\text{con}} + K_{\text{dp}}\{v_o(t - T_h) - v_o(t)\} + K_{\text{di}}\{\rho_i(t - T_h) - \rho_i(t)\} \tag{12}$$

where, K_{dp} and K_{di} are gains related to time-delay controller. The only information needed to generate delayed signals $v_o(t - T_h)$ and $\rho_i(t - T_h)$ is the switching period T_s of the system since $T_h = \frac{T_s}{2}$. As the ideal time delay introduces infinite dimension in the system hence making its systematic stability analysis challenging, it is realized by a first order all pass filter given in Fig. 7(b) making the stability analysis and the determination of the stability domain an easy task. In time-domain (i.e., waveforms), the time delay will be shown as phase delay.

The transfer function of the all pass filter of Fig. 7 is given by

$$\frac{V_d(s)}{V(s)} = \frac{1 - R_d C_d s}{1 + R_d C_d s} \tag{13}$$

There are two time delay modules used to implement the controller. Therefore, the original four-dimensional system is now six-dimensional piecewise-linear system. The stability analysis will be done by the same method used for the original PI controlled system. The control domain of the gains (K_{dp}, K_{di}) is found by following the maximum eigenvalue(s) with the variation of the parameters.

TABLE 1 Design-1: Parameters of the converter.

Specifications	Parameters
Input voltage, V_s = 25 V–32 V	L_r = 48 μH, C_r = 0.33 μF
Output voltage, v_o = 12 V ± 1%	C_f = 47 μF
Output power, P_o = 24 W–36 W	R_L = 4 Ω – 6 Ω
Switching frequency, f_s = 50 kHz	$Z_0 = \sqrt{\frac{L_r}{C_r}}$ = 12 Ω
Resonant frequency, $f_r \approx$ 40 kHz	K_p = 1, K_i = 5000 s^{-1}
f_s/f_r = 1.25, $Q_s = \frac{Z_0}{R_L} \approx 2 - 3$	V_U = 2.0 V, V_L = −2.0 V

5 | DESIGN OF THE CONVERTER AND APPLICATION OF THE HPTD CONTROLLER

To set design parameters, different operating conditions for different applications are considered. There are several designs which are listed below:

5.1 | Design-1: Operation Mode-I, Moderate gain, $\frac{f_s}{f_r} \approx 1.25$

In this design (Table 1), we can achieve ZVS for both legs of the full-bridge configuration shown in Fig. 1. Typical steady-state symmetric waveforms are shown in Fig. 3(a).

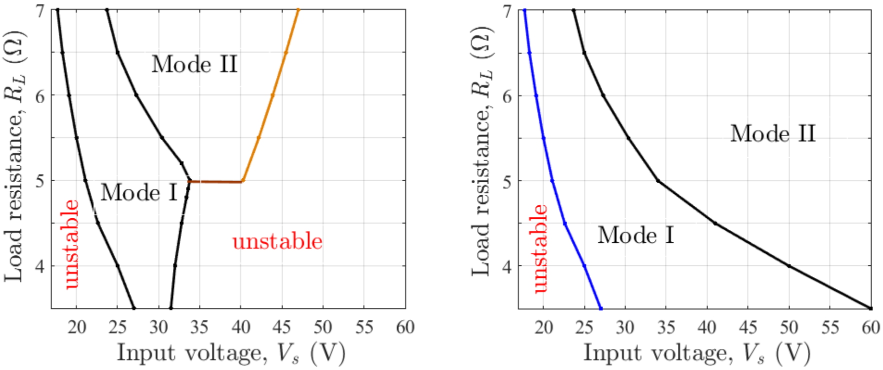

(a)

(b)

FIGURE 8 Stable region in the $V_s - R_L$ parameter space (a) PI control and (b) HPTD feedback control. (color online)

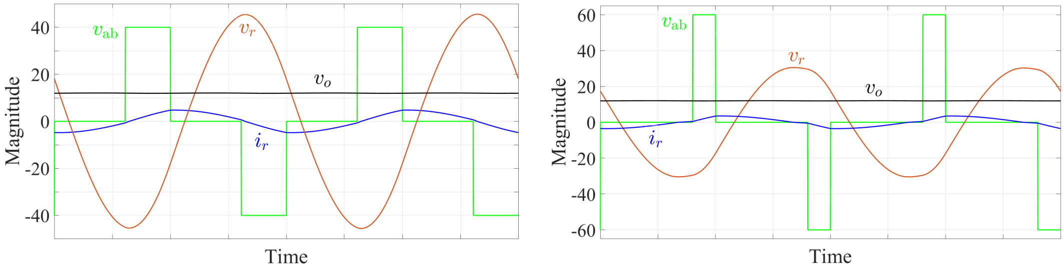

(a)

(b)

FIGURE 9 Key waveforms with HPTD ($K_{\rm dp} = 0.1$ and $K_{\rm di} = 10$) at (a) $V_s = 40$ V, $R = 4\ \Omega$ (Mode-I) and (b) $V_s = 60$ V, $R = 6\ \Omega$ (Mode-II). Other parameters are given in Table 1. (color online)

As shown in Fig. 4(b), the variation of duty ratio is large with the variation of load. To design the controller parameters, the worst case scenario is considered when $V_s = 32$ V and $R_L = 6\ \Omega$ and a stability curve has been drawn in $K_p - K_i$ parameter space (Fig. 6(a)). From that $K_p = 1$ and $K_i = 5000\ s^{-1}$ have been chosen. The operating region in the $V_s - R_L$ parameter space is shown in Fig. 8(a) where at $R_L = 5\ \Omega$, the operation mode is changed from Mode-I to

Mode-II with the variation of the input voltage. Now using HPTD feedback control with the gains of the time-delay controller in the range of $K_{\text{dp}} = 0.01 - 0.1$ and $K_{\text{di}} = 5 - 15$, the instability has been avoided (Fig. 8(b)) in the $V_s - R_L$ parameter space. After applying HPTD feedback control, the key waveforms are shown for different input voltages and loads as shown in Fig. 9. Note that the system was unstable with PI controller at these two operating conditions.

TABLE 2 Design-2: Parameters of the converter

Specifications	Parameters
Input voltage, V_s = 15 V–60 V	L_r = 48 μH, C_r = 0.2 μF
Output voltage, v_o = 12 V ±1%	C_f = 47 μF,
Output power, P_o = 5 W–50 W	R_L = 3 Ω – 30 Ω
Switching frequency, f_s = 50 kHz	$Z_0 = \sqrt{\frac{L_r}{C_r}} = 15.5\ \Omega$
Resonant frequency, $f_r \approx 51.4$ kHz	$K_p = 1$, $K_i = 2000\ s^{-1}$
$f_s/f_r = 0.9734$, $Q_s = \frac{Z_0}{R_L} \approx 0.5 - 5$	V_U = 2.0 V, V_L = −2.0 V

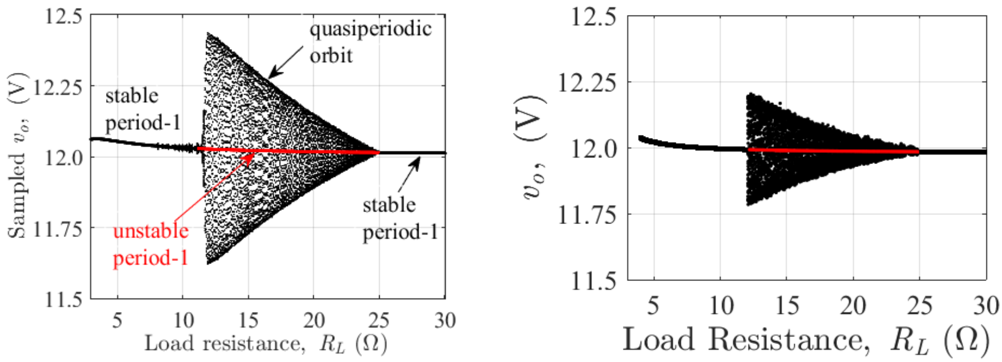

(a) (b)

FIGURE 10 Bifurcation diagram with the variation of the load resistance at (a) $V_s = 15$ V, and (b) $V_s = 60$ V with PI control. The red line indicates unstable period-1 orbit. Other parameters are given in Table 2. (color online)

5.2 | Design-2: Operation Mode-II, High gain, $\frac{f_s}{f_r} \approx 1$

In this design (Table 2), the variation of input voltage and load are large. As shown in Fig. 4(c) and (e), if the system is operated in the region of $\frac{f_s}{f_r} = 0.95$ to $\frac{f_s}{f_r} = 1.05$, then the variation in the duty ratio is small with the variation of load. In both the cases the duty ratio is increasing with the decreasing of the input voltage. As shown in Fig. 10(a), at high voltage gain (≈ 0.8) with the increasing value of the load resistance (low load), the system exhibits Neimark-Sacker bifurcation i.e., slow-timescale oscillations at $R_L = 11.2\ \Omega$. The calculated maximum eigenvalues are shown in Table 3. But using HPTD feedback control with gains in the range of $K_{\text{dp}} = -1$ to -10 and $K_{\text{di}} = 10 - 20$, the instability has been suppressed which is shown in Fig. 11(a). Similarly at low gain (≈ 0.25, $V_s = 60$ V), with the increasing value of the load resistance (low load) the system shows Neimark-Sacker bifurcation (Fig. 10(b)) which has been avoided by HPTD

TABLE 3 Eigenvalues with the variation of R_L (Ω) corresponding to Fig. 10(a).

R_L	Orbit	Mode seq.	Fixed point	Eigenvalues
3.0	stable	1 2 3 2 1 6	[−1.7801 −96.5528 12.0609 −0.4361]	0.7292 ± 0.5237j (≈ 0.8978), 0.6850, 0.9699
11.1	stable	1 2 3 2 1 6	[−1.3896 −20.5579 12.0283 −0.2871]	0.8500 ± 0.5264j (≈ 0.9998, 0.1469, 0.9691
11.2	unstable	1 2 3 2 1 6	[−1.3831 −20.3356 12.0281 −0.2871]	0.8504 ± 0.5266j (≈ 1.0002), 0.1439, 0.9691
24.9	unstable	1 2 3 2 1 6	[−0.9317 −7.2396 12.0144 −0.2885]	0.8723 ± 0.5381j (≈ 1.0249), 0.9692, 0.0
25.0	stable	1 7 2 3 2 7 1 6	[−0.9299 −7.2001 12.0143 −0.2885]	0.8268 ± 0.5145j (≈ 0.9739), 0.9688, 0.0
30.0	stable	1 7 2 3 2 7 1 6	[−0.8168 −6.0000 12.0124 −0.2262]	0.5435 ± 0.6437j (≈ 0.8417), 0.9633, 0.0

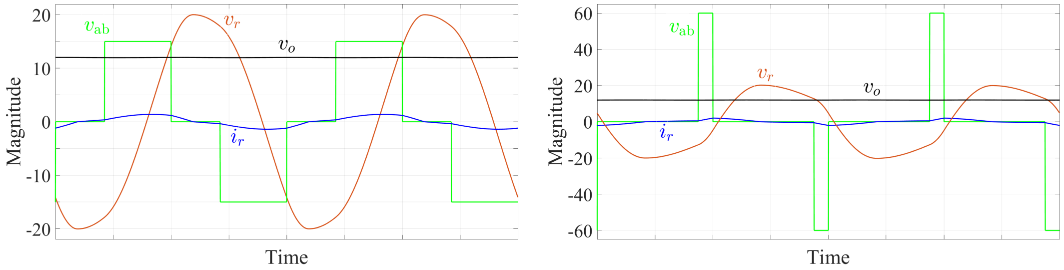

(a)

(b)

FIGURE 11 Key waveforms with HPTD ($K_{dp} = -1$ and $K_{di} = 10$) at (a) $V_s = 15$ V, $R = 15$ Ω (Mode-II) and (b) $V_s = 60$ V, $R = 15$ Ω (Mode-II). Other parameters are given in Table 2. (color online)

feedback which is shown in Fig. 11(b).

5.3 | Design-3: Operation Mode-II, Moderate gain, $\frac{f_s}{f_r} \approx 0.9$

In this design (Table 4), the switching frequency is below the resonant frequency, therefore we can achieve ZCS for both legs. The stable region in the $V_s - R_L$ parameter space has been identified (Fig. 12(a)). But using HPTD feedback control with the gains in the range of $K_{dp} = -0.01$ to -0.1 and $K_{di} = 5$–15. The instability has been avoided as depicted in

TABLE 4 Design-3: Parameters of the converter

Specifications	Parameters
Input voltage, V_s = 20 V−36 V	L_r = 40 μH, C_r = 0.2 μF
Output voltage, v_o = 12 V ±1% V	C_f = 47 μF
Output power, P_o = 10 W−24 W	R_L = 6 Ω − 15 Ω
Switching frequency, f_s = 50 kHz	$Z_0 = \sqrt{\frac{L_r}{C_r}}$ = 14.14 Ω
Resonant frequency, f_r = 56.27 kHz	K_p = 5, K_i = 5000 s^{-1}
f_s/f_r = 0.89, $Q_s = \frac{Z_0}{R_L} \approx 1-2$	V_U = 2.0 V, V_L = −2.0 V

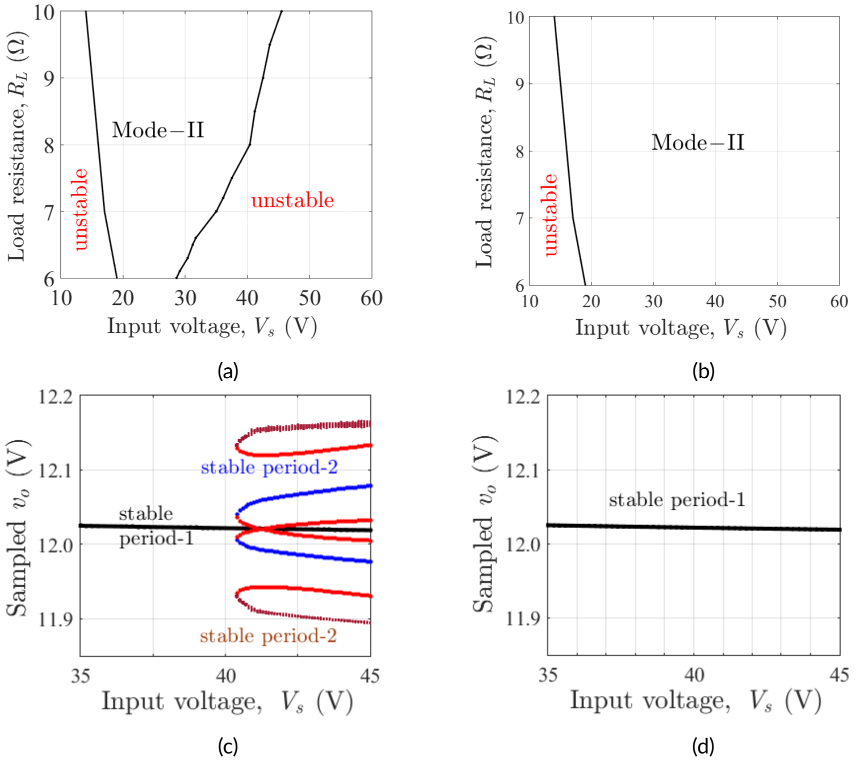

FIGURE 12 Stable region in the $V_s - R_L$ parameter space with (a) PI control, (b) HPTD control. Bifurcation diagram with the variation of input voltage at $R_L = 8\ \Omega$ with (c) PI control, (d) HPTD control. (color online)

Fig. 12(b). As showed in the Fig. 12(c), at high load resistance ($R_L = 8\ \Omega$), with the increasing value of the input voltage there is a range in which two stable period-2 orbits (marked by blue and brown) co-exist with nominal period-1 orbit (marked by black). The two period-2 orbits come into existence at $V_s = 40.4$ V by saddle-node bifurcation. The two unstable period-2 orbits are marked by red. The change in maximum eigenvalue with the variation of input voltage is

TABLE 5 Eigenvalues with the variation of V_s corresponding to Fig. 12(c)

V_s (V)	Orbit	Mode seq.	Fixed point	Eigenvalues
35.0	stable period-1	1 2 3 2 1 6	[−2.5153 −22.4363 12.0250 1.1318]	−0.8574 ± 0.1495j, 0.3382, 0.9804
40.0	stable period-1	1 2 3 2 1 6	[−2.6418 −20.4888 12.0218 1.2486]	−0.8768 ± 0.0627j, 0.3315, 0.9804
40.4	stable period-2	1 2 3 2 1 6...	[−3.4722 −35.0141 12.0059 1.2093]	0.0755, 0.6454, 0.8661, 0.9612
40.4	unstable period-2	1 2 3 2 1 6...	[−1.5419 −14.1190 12.0363 1.2173]	0.0782, 0.5179, 0.9613, 1.0941
40.4	stable period-2	1 2 3 2 1 6...	[−2.7703 −20.3473 11.9302 1.2130]	0.0756, 0.6441, 0.8683, 0.9612
40.4	unstable period-2	1 2 3 2 1 6...	[−2.7948 −20.7395 11.9340 1.2148]	0.0782, 0.5184, 0.9613, 1.0941
45.0	stable period-1	1 2 3 2 1 6	[−2.7333 −18.9380 12.0190 1.3383]	−0.8437 ± 0.2700j, 0.3265, 0.9804

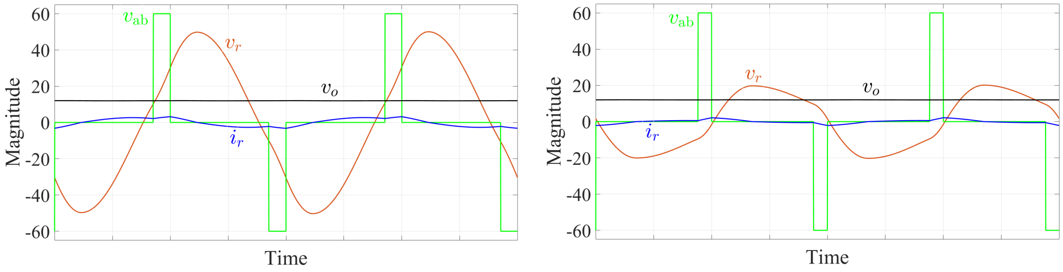

(a)

(b)

FIGURE 13 Key waveforms with HPTD ($K_{dp} = -0.1$ and $K_{di} = 10$) at (a) $V_s = 60$ V, $R = 6$ Ω (Mode-II) and (b) $V_s = 60$ V, $R = 15$ Ω (Mode-II). Other parameters are given in Table 4. (color online)

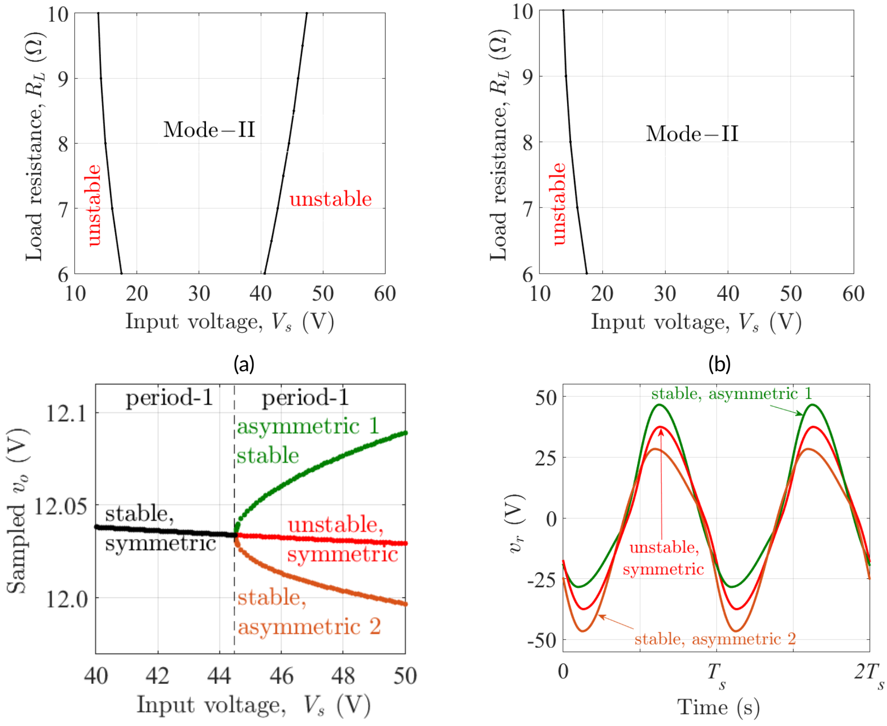

(d)

FIGURE 14 (a) Stable region in the $V_s - R_L$ parameter space with (a) PI control, (b) HPTD control. (c) Bifurcation diagram with the variation of input voltage at $R_L = 8$ Ω with PI control, (d) Waveforms of resonant capacitor voltage v_r at $V_s = 50$ V. (color online)

shown in Table 5. By HPTD control only the nominal period-1 orbit exists (Fig. 12(d)). After applying HPTD feedback control, the key waveforms are shown for different input voltages and loads as shown in Fig. 13. Note that the system was unstable with PI controller at these two operating conditions.

Now keeping fixed all other parameters in Table 4, if we change the value of filter capacitor $C_f = 27$ μF, the stable

TABLE 6 Eigenvalues with the variation of V_s corresponding to Fig. 14(c)

V_s (V)	Period-1 Orbit	Mode seq.	Fixed point	Eigenvalues
40.0	stable symmetric	1 2 3 2 1 6	[−2.6401 −20.5280 12.0381 1.2842]	0.3111 ± 0.8142j, 0.3237, 0.9804
50.0	stable asymmetric 1	1 2 3 2 1 6	[−1.8089 −19.2826 12.0890 1.3622]	−0.3039 ± 0.8776j, 0.2570, 0.9804
50.0	stable asymmetric 2	1 2 3 2 1 6	[−3.2207 −24.8998 11.9967 1.3610]	−0.3035 ± 0.8778j, 0.2571, 0.9804
50.0	unstable symmetric	1 2 3 2 1 6	[−2.8012 −17.7149 12.0293 1.4421]	0.2431, 0.3155, 0.9803, 3.2047

region in the $V_s - R_L$ parameter space (Fig. 14(a)) is delimited by symmetry breaking bifurcation. At $R_L = 8\ \Omega$, with the variation of input voltage, the stable symmetric period-1 orbit becomes unstable at $V_s = 44.53$ V (Fig. 14(c)), and two stable asymmetric period-1 orbits are created. The waveforms of unstable symmetric and stable asymmetric resonant capacitor voltages at $V_s = 50$ V are shown in (Fig. 14(d)) starting from different initial conditions. As shown in Table 6, the calculated maximum eigenvalue passes through +1 as the symmetric period-1 orbit becomes unstable and the resulting bifurcation is known as pitchfork or symmetry-breaking. Using HPTD feedback control with gains in the range of $K_{\text{dp}} = 1$ to 2 and $K_{\text{di}} = 25 - 50$, the instability has been avoided (Fig. 14(b)).

6 | DISCUSSION

In this study the components used in the circuit (Fig. 1) are considered ideal. In reality, there are paracitics with inductor and capacitor in the form of series resistance. To ease the ZVS, capacitors are used in parallel to each switch for leg A and leg B. For the full bridge switch circuit, the dead-time is also not considered. In case of all switches and rectifier diode bridge, the resistances are omitted. Moreover, for the gate driver circuit, the controlling resistors are avoided in the simulation.

The instabilities shown in this paper for different operation modes exhibiting different phenomena are typical nonlinear behavior of the overall system (power and control stages). The system is modelled by considering switching nonlinearity in the state equations of the energy storing elements. All these nonidealities, only shift the occurrence of the main phenomena with the variation of the parameters. The power level and switching frequency of the switches can also be increased to kW and MHz range separately. In this case, those phenomena reported in this will also occur in the parameter space because the stable regions are delimited by the variation of the parameters in a well designed system. In this study, the aim is show that how bifurcation control can be used to extend the stability margin of a switching converter working in a specified range of input voltage and output load for which it was designed.

7 | CONCLUSION

In this paper, for different operating conditions of fixed frequency phase shift modulated series resonant converter, the stable regions in the $V_s - R_L$ parameter space have been found analytically using the nonlinear switched model. The desired stable regions are delimited by different types of instabilities which are identified by the calculation of maximum eigenvalue with the variation of parameters. Later these slow- and fast-timescale instabilities have been avoided using Half-Period Time Delay (HPTD) feedback control by choosing the controller gains from domain of control appropriately. Therefore, the reliable period-1 operation range for different operating conditions in the $V_s - R_L$ parameter space has been increased drastically. The three types of instabilities commonly occur in this class of converter which can be avoided by single HPTD control considering the symmetry in the waveforms. This study can be extended to other topologies as the dimension and number of topological modes within a switching cycle will not pose any limitation on the stability analysis method.

references

[1] Alatai S, Salem M, Delgado MT, Ishak D, Kamarol M. Modelling a five-level LLC resonant converter for bidirectional battery application. International Journal of Circuit Theory and Applications 2024;p. 1–25.

[2] Yu SY, Chen R, Viswanathan A. Survey of Resonant Converter Topologies. Power Supply Design Seminar, Texas Instruments; 2018.

[3] Saadabad NZ, Nasiri A, Nekoui J. A new three-port DC/DC converter with soft switching, for PV applications. International Journal of Circuit Theory and Applications 2024 June;Early access.

[4] Shen Y, Wang H, Shen Z, Yang Y, Blaabjerg F. A 1-MHz Series Resonant DC-DC Converter With a Dual-Mode Rectifier for PV Microinverters. IEEE Transactions on Power Electronics 2019 July;34(7):6544–6564.

[5] Tian D, Tang Y, Shi Z. Design and optimization of 30 kW CLLLC resonant converter for vehicle-to-grid applications. International Journal of Circuit Theory and Applications 2024 July;Early access.

[6] Mudiyanselage GA, Keshmiri N, Emadi A. A Review of DC-DC Resonant Converter Topologies and Control Techniques for Electric Vehicle Applications. IEEE Open Journal of Power Electronics early access, 2024;.

[7] Deshmukh S, Iqbal A, Islam S, Khanb I, Marzband M, Rahmanb S, et al. Review on classification of resonant converters for electric vehicle application. Energy Reports 2022 November;8:1091–1113.

[8] Shahsevani J, Beiranvand R. Application-Oriented Review of the LLC-Based Resonant Converters. IEEE Access 2024 April;12:52687–52726.

[9] Salema M, Jusoh A, Idris NRN, Das HS, Alhamrouni I. Resonant power converters with respect to passive storage (LC) elements and control techniques: An overview. Renewable and Sustainable Energy Reviews 2018;91:504–520.

[10] Jiang X, Chen Y, Zhang B, Qiu D, Xie F. Harmonic analysis of VHF resonant converter based on equivalent nonlinear controlled model. International Journal of Circuit Theory and Applications 2022;50(7):2615–2630.

[11] Olm JM, Biel D, Spinetti-Rivera M, Fossas E. Harmonic balance-based control of a boost DC/AC converter. International Journal of Circuit Theory and Applications 2012;40:777–792.

[12] El Aroudi A, Benadero L, Ponce E, Olalla C, Torres F, Martínez-Salamero L. Nonlinear Dynamic Modeling and Analysis of Self-Oscillating H-Bridge Parallel Resonant Converter Under Zero Current Switching Control: Unveiling Coexistence of Attractors. IEEE Transactions on Circuits and Systems I: Regular Papers 2019 April;66(4):1657–1667.

[13] Mandal K, Chakraborty C, Abusorrah A, Al-Hindawi MM, Al-Turki Y, Banerjee S. An automated algorithm for stability analysis of hybrid dynamical systems. The European Physical Journal Special Topics 2013;222(3-4):757–768.

[14] Mandal K, Banerjee S, Chakraborty C. A New Algorithm for Small-Signal Analysis of DC–DC Converters. IEEE Transactions on Industrial Informatics 2014 February;10(1):628–636.

[15] Mandal K, Chakraborty C, Abusorrah A, Al-Hindawi MM, Al-Turki Y, Banerjee S. An automated algorithm for stability analysis of hybrid dynamical systems. The European Physical Journal Special Topics 2013 July;222(3-4):757–768. Doi: 10.1140/epjst/e2013-01879-x.

[16] Mandal K, SBSDS - Stability and Bifurcation of Switched Dynamical System; last accessed on 14th October, 2023. https://dsweb.siam.org/Software/pager/225/page/4.

[17] Dranga O, Buti B, Nagy I. Stability analysis of a feedback controlled resonant DC-DC converter. IEEE Transactions on Industrial Electronics 2003 February;50(1):141–152.

[18] Mandal K, Banerjee S, Chakraborty C. Symmetry-Breaking Bifurcation in Series-Parallel Load Resonant DC-DC Converters. IEEE Transactions on Circuits and Systems-I 2013 March;60(3):778–787.

[19] Mandal K, El Aroudi A, Abusorrah A, Al-Hindawi MM, Al-Turki Y, Giaouris D, et al. Nonlinear Modeling and Stability Analysis of Resonant DC-DC Converters. IET Power Electronics 2015 December;8(12):2492–2503.

[20] Iu HHC, Robert B. Control of Chaos in a PWM Current-Mode H-Bridge Inverter Using Time-Delayed Feedback. IEEE Transactions on Circuits and Systems-I: Fundamental Theory and Applications 2003 August;50(8):1125–1129.

[21] El Aroudi A, Leyva R. Quasi-periodic route to chaos in a PWM voltage-controlled DC-DC boost converter. IEEE Transactions on Circuits and Systems I: Fundamental Theory and Applications 2001 August;48(8):967–978.

[22] Banerjee S, Grebogi C. Border collision bifurcations in two-dimensional piecewise smooth maps. Physical Review E 1999 April;59(4).

[23] Benadero L, El Aroudi A, Ponce E. Delay effects on the limit cycling behavior in resonant inverters with state feedback. Nonlinear Theory and Its Applications, IEICE 2019;10(4):337–356.

[24] El Aroudi A, Huang J, Al-Numay MS, Li Z. On the Coexistence of Multiple Limit Cycles in H-Bridge Wireless Power Transfer Systems With Zero Current Switching Control. IEEE Transactions on Circuits and Systems I: Regular Papers 2020;67(5):1729–1739.

[25] Bandyopadhyay A, Mandal K, Parui S. A Filippov method based analytical perspective on stability analysis of a DC-AC H-bridge inverter with nonlinear rectifier load. International Journal of Circuit Theory and Applications 2022 May;50(5):1686–1708.

[26] Wu R, Zhang X, Jiang W. Bifurcation analysis and control in a DC–AC inverter with PID controller. International Journal of Circuit Theory and Applications 2024 August;Early access.

[27] El Aroudi A, Benadero L, Ponce E, Olalla C, Torres F, Martinez-Salamero L. Suppression of Undesired Attractors in a Self-Oscillating H-Bridge Parallel Resonant Converter Under Zero Current Switching Control. IEEE Transactions on Circuits and Systems II: Express Briefs 2019 April;66(4):692–696.

[28] Pyragas K. Continuous Control of chaos by self-controlling feedback. Physics Letters A 1992;120:421–428.

[29] Batlle C, Fossas E, Olivar G. Stabilization of Periodic Orbits of the Buck Converter by Time-Delayed Feedback. International Journal of Circuit Theory and Applications 1999 November;27(5):617–631.

[30] Iu HHC, Robert B. Control of chaos in a PWM current-mode H-bridge inverter using time-delayed feedback. IEEE Transactions on Circuits and Systems I 2003;50(8):1125–1129.

[31] El Aroudi A, Orabi M. Dynamics of PFC power converters subject to time-delayed feedback control. International Journal of Circuit Theory and Applications 2012;40(1):15–35.

[32] Lu WG, Zhou LW, Luo QM, Zhang XF. Filter based non-invasive control of chaos in Buck converter. Physics Letters A 2008;372(18):3217–3222.

[33] Rodriguez E, Alarcón E, Iu HHC, El Aroudi A. A Frequency Domain Approach for Controlling Fast-Scale Instabilities in Switching Power Converters. International Journal of Bifurcation and Chaos 2015 October;25(11):1550141.

[34] Lu WG, Luo-Wei Z, Quan-Ming L, Jun-Ke W. Non-invasive chaos control of DC-DC converter and its optimization. International Journal of Circuit Theory and Applications 2011 February;39(2):159–174.

[35] El Aroudi A, Haroun R, Cid-Pastor A, Martinez-Salamero L. Suppression of line frequency instabilities in PFC AC-DC power supplies by feedback notch filtering the pre-regulator output voltage. IEEE Transactions on Circuits and Systems I: Regular Papers 2013;60(3):796–809.

[36] Chen G, Yu X. On time-delayed feedback control of chaotic systems. IEEE Transactions on Circuits and Systems-I: Fundamental Theory and Applications 1999 June;46(6):767–772.

[37] Nakajima H, Ueda Y. Half-period delayed feedback control for dynamical systems with symmetries. Physical Review E 1998 August;58(2):1757–1763.

[38] Lee FC. High-frequency quasi-resonant converter technologies. Proc of IEEE 1988 April;76(4):377–390.

[39] Batarseh I. Resonant converter topologies with three and four energy storage elements. IEEE Transactions on Power Electronics 1994 January;9(1):64–73.

[40] Wang CM. Novel zero-voltage-transition PWM DC-DC converters. IEEE Transactions on Industrial Electronics 2006 February;53(1):254–262.

[41] Lakshminarasamma N, Masihuzzaman M, Ramanarayanan V. Steady-State Stability of Current-Mode Active-Clamp ZVS DC-DC Converters. IEEE Transactions on Power Electronics 2011 May;26(5):1295–1304.

[42] Nathan BS, Rammarayanan V. Analysis, Simulation and Design of Series Resonant Converter for High Voltage Applications. Goa, India: IEEE International Conference on Industrial Technology; 2000. p. 682–692.

[43] Ahmadian HM, Tahami F, Karimpour A, Pariz N. Hybrid Control of DC-DC Series Resonant Converters: The Direct Piecewise Affine Approach. IEEE Transactions on Power Electronics 2015 March;30(3):1714–1723.

[44] Afshang H, Tahami F, Molla-Ahmadian H. Hybrid control of the dc–dc SRC operating below resonance. IET Power Electronics 2017 January;10(1). Early access.

[45] Kong J, Sun R, Xu M, Liu X. Half-bridge secondary series resonant converter control for full voltage range. International Journal of Circuit Theory and Applications 2024 February;Early access.

[46] Shi Z, Tang Y, Davari P. On-board charger applications: A new hybrid control strategy for bidirectional CLLC resonant converter. International Journal of Circuit Theory and Applications 2024 January;Early access.

[47] Li X, Zhan S, Yang Z, Guo F, Liao H. Improved linear active disturbance rejection control for double active bridge series resonant converter with high voltage gain. International Journal of Circuit Theory and Applications 2024 June;Early access.

[48] Liu B, Han M, Zhou Q, Liu Y. Soft-switching boundary and piecewise control of LLC converter with hybrid modulation. International Journal of Circuit Theory and Applications 2024 August;Early access.

[49] Nalbant MK. Phase Modulated PWM Topology with ML4818. Application Note 42026. Fairchild Semiconductor; 1996.

[50] Dionizio AA, Sampaio LP, da Silva SAO. Generalized state-space averaging modeling to fourth-order power converters operating in DCM. International Journal of Circuit Theory and Applications 2024 June;Early access.

[51] Tian S, Lee FC, , Li Q. A Simplified Equivalent Circuit Model of Series Resonant Converter. IEEE TRANSACTIONS ON POWER ELECTRONICS 2016 May;31(5):3922–3931.

[52] Li X, Zhang Y, Chen S, Tang Y, Zhang X. Small-Signal Modeling for Phase-Shift Controlled Resonant Converters. IEEE Transactions on Industrial Electronics 2021 November;68(11):11026–11034.